Title

Termination switching of antiferromagnetic proximity effect in topological insulator

Journal

Science Advances, 6(33)

ISSN

2375-2548

Authors

Yang, Chao-Yao

Pan, Lei

Grutter, Alexander J

et al.

Publication Date

2020-08-14

DOI

10.1126/sciadv.aaz8463

Peer reviewed

CONDENSED MATTER PHYSICS

Termination switching of antiferromagnetic proximity effect in topological insulator

Chao-Yao Yang[1]*†, Lei Pan[1]*, Alexander J. Grutter[2]*, Haiying Wang[3], Xiaoyu Che[1], Qing Lin He[1,4], Yingying Wu[1], Dustin A. Gilbert[2,5], Padraic Shafer[6], Elke Arenholz[6,7], Hao Wu[1], Gen Yin[1], Peng Deng[1], Julie Ann Borchers[2], William Ratcliff II[2,8], Kang L. Wang[1,9,10†]

This work reports the ferromagnetism of topological insulator, $(Bi,Sb)_2Te_3$ (BST), with a Curie temperature of approximately 120 K induced by magnetic proximity effect (MPE) of an antiferromagnetic CrSe. The MPE was shown to be highly dependent on the stacking order of the heterostructure, as well as the interface symmetry: Growing CrSe on top of BST results in induced ferromagnetism, while growing BST on CrSe yielded no evidence of an MPE. Cr-termination in the former case leads to double-exchange interactions between Cr^{3+} surface states and Cr^{2+} bulk states. This Cr^{3+}-Cr^{2+} exchange stabilizes the ferromagnetic order localized at the interface and magnetically polarizes the BST Sb band. In contrast, Se-termination at the CrSe/BST interface yields no detectable MPE. These results directly confirm the MPE in BST films and provide critical insights into the sensitivity of the surface state.

INTRODUCTION

Since the realization of the quantum anomalous Hall effect (QAHE) in magnetic topological insulators (TIs) (*1*–*4*), there has been enormous interest in bringing quantum transport effects to room temperature. One of the most promising approaches to achieve room temperature quantum transport has been the use of magnetic proximity effects (MPEs) to induce magnetic order in a TI by coupling it to an adjacent magnetically ordered material (*5*–*11*). The coupling between the TI and the magnetically ordered material may stabilize high-temperature magnetic order in TI through the exchange interaction while preserving the topologically protected surface states. Current effort has been devoted to studying interfacial exchange coupling and identifying the conditions to maximize the MPE, and previous works have demonstrated that growing magnetic insulators such as EuS (*10*) and rare-earth iron garnets adjacent to TI results in MPE-induced ferromagnetism in the TI with Curie temperatures ranging from 100 (*6*–*9*) to 400 K (*5*). Recently, antiferromagnets (AFMs) with uncompensated surface spins have been shown to ferromagnetically couple in the basal plane, making them attractive candidates for realizing the MPE (*12*–*14*). These AFM-induced MPEs have been used in TI heterostructures, resulting in ferromagnetism (*14*–*16*), exchange bias (*14*), chiral spin structures, and the geometric Hall effect (*15*). In addition to the demonstrated ability to readily tune the magnetic and transport properties of the TI, AFMs have a number of technological advantages such as ultrafast dynamics, nonexistent dipole fields, and robustness against external field perturbations (*17*, *18*). These ultrafast dynamics have recently been realized in Cr_2O_3-based heterostructures, where spin currents were generated through AFM magnons (*19*). Although combining AFM and TI layers opens new horizons for quantum spintronics (*20*), the origins of MPEs at the atomic level remain unclear and are challenging to probe directly because the signal from interfacial spin torque effects may come alternatively from a response to the electrical probing (*21*). Therefore, an element-specific investigation to study the MPE-induced magnetism in TI is required to fundamentally understand the physical picture behind the observable phenomenologies and unveil the origin of MPEs at TI heterointerfaces.

RESULTS

Structural, magnetic, and transport properties of CrSe/BST/CrSe epitaxial trilayer

Figure 1 (A and B) shows the crystalline and magnetic structure of the CrSe used in this work. CrSe crystallizes in a hexagonal NiAs structure, and the magnetic ordering has been proposed to have an umbrella-like, noncollinear AFM structure, with a moment tilting out of the basal plane (*22*, *23*). The Néel temperature of the bulk CrSe was found to be 270 K (see fig. S1). Both the CrSe and TI [$(Bi_{0.25}Sb_{0.75})_2Te_3$ (BST)] films were grown in the (0001) orientation using molecular beam epitaxy and fabricated into a Hall bar (1 mm by 0.5 mm) afterward, as described in the Materials and Methods. Figure 1C shows a cross-sectional scanning transmission electron microscopy (STEM) image for a CrSe/TI/CrSe trilayer structure and the corresponding energy-dispersive spectroscopic (EDS) mapping for Cr, Te, Bi, Te, and Ga in sequence. The atomically resolved STEM micrographs reveal the expected quintuple-layered structure of the BST, along with sharp, high-quality interfaces. We note that the in-plane orientation of the BST and top CrSe do not match that of the bottom CrSe layer, likely because of the van der Waals structure of the BST layers. Elemental mapping using EDS across interfaces reveals a homogeneous elemental distribution within the layers, separated by the interfaces. To investigate the MPE-induced magnetism in the BST, we performed magnetotransport measurements on the structurally symmetric CrSe(5)/BST(6)/CrSe(5) trilayer after 1-T field

[1]Department of Electrical and Computer Engineering, University of California, Los Angeles, CA 90095, USA. [2]NIST Center for Neutron Research, National Institute of Standards and Technology, Gaithersburg, MD 20899-6102, USA. [3]College of Physics and Material Science, Henan Normal University, Xinxiang 453007, China. [4]International Center for Quantum Materials, School of Physics, Peking University, Beijing 100871, China. [5]Department of Materials Science and Engineering, University of Tennessee, Knoxville, TN 37996, USA. [6]Advanced Light Source, Lawrence Berkeley National Laboratory, Berkeley, CA 94720, USA. [7]Cornell High Energy Synchrotron Source, Ithaca, NY 14853, USA. [8]Department of Materials Science and Engineering, University of Maryland, College Park, MD 20742, USA. [9]Department of Materials Science and Engineering, University of California, Los Angeles, CA 90095, USA. [10]Department of Physics and Astronomy, University of California, Los Angeles, CA 90095, USA.
*These authors contributed equally to this work.
†Corresponding author. Email: cyyang8611@gmail.com (C.-Y,Y); wang@seas.ucla.edu (K.L.W.)

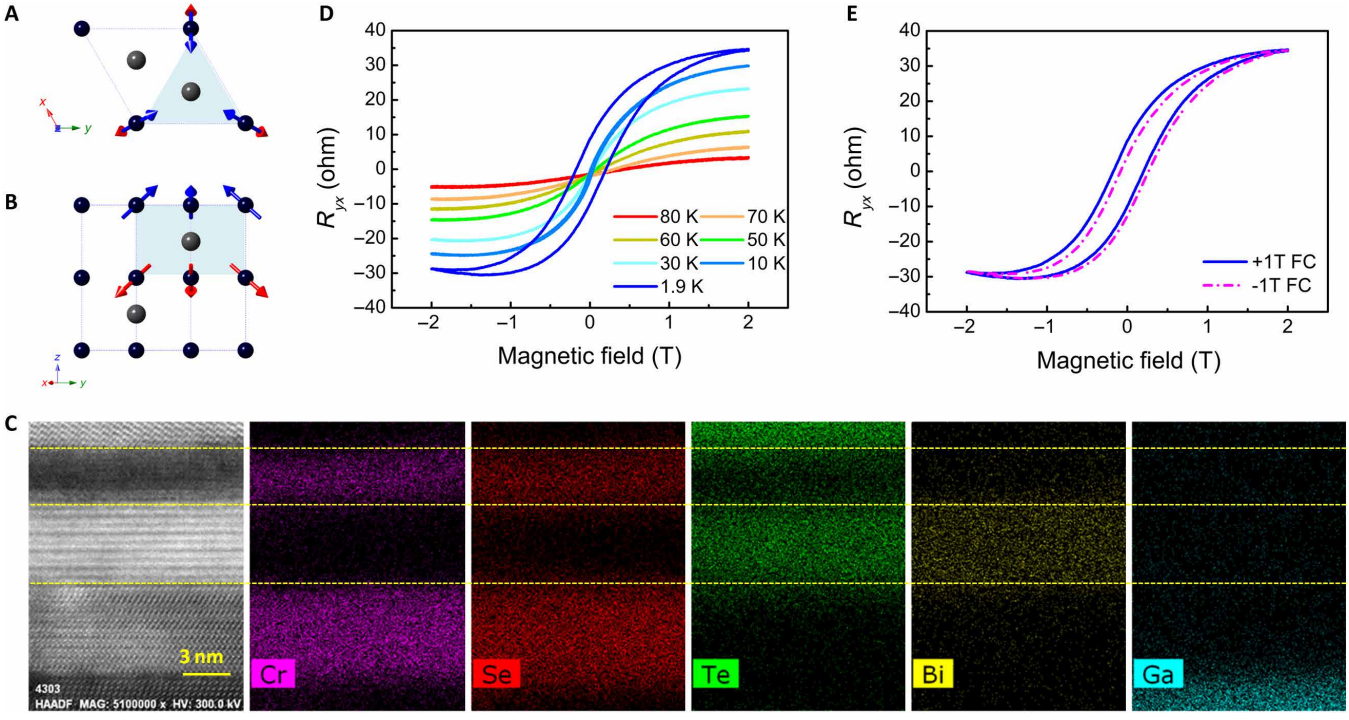

Fig. 1. Microstructure and magnetotransport of the CrSe/BST/CrSe trilayer. (**A**) Top view and (**B**) cross-sectional view of crystalline and magnetic structure of AFM CrSe. Region highlighted by blue shows the magnetic unit of AFM in the CrSe crystal. (**C**) STEM image of the GaAs/CrSe/BST/CrSe/Te structure, along with its EDS images for Cr, Se, Te, Bi, and Ga in sequence. (**D**) Temperature-dependent R_{yx} curves of the CrSe(5)/BST(6)/CrSe(5) trilayer acquired by applying 1-T field cooling (FC). (**E**) Exchange bias (~40 mT) at 1.9 K achieved on the horizontal shift on the R_{yx} by applying an opposite 1-T field cooling.

cooling from room temperature to low temperatures, and the result is shown in Fig. 1D, where the unit of thickness is in nanometers. In addition to a clear ferromagnetic hysteresis loop, the trilayer exhibits an exchange bias of approximately 40 mT, as shown in Fig. 1E. Because the CrSe layer is much more insulating than BST (see fig. S2), nearly all the current from the magnetotransport flows through the BST, allowing the observed anomalous Hall effect (AHE) to be attributed to the BST layer. To further eliminate the possibility that the AHE originates in the noncollinear AFM of the CrSe, we performed AHE measurements on a bare CrSe film, which exhibited a linear nonhysteretic response (see fig. S3). Thus, the emergence of an AHE in the transport indicates that the BST becomes magnetically polarized and is thus strongly coupled to the CrSe (*14*, *24*, *25*). The temperature dependence of the AHE shown in Fig. 1D reveals a clear transition in the MPE-induced ferromagnetism, with both coercive field (H_c) and anomalous Hall resistance (R_{AHE}) decreasing with increasing temperature up to 120 K (see fig. S4). Both the high transition temperature of the AHE and the exchange bias indicate a strong exchange coupling across the BST/CrSe interface (*14*).

Interfaces with asymmetric magnetic property identified by bilayer characterizations

Although the ferromagnetism arising from the two interfaces of the CrSe(5)/BST(6)/CrSe(5) trilayer is expected to contribute equally because of its geometric symmetry, unexpected results emerge when varying the stacking order between CrSe and BST. Representative temperature-dependent Hall data of GaAs/CrSe(5)/BST(6) and GaAs/BST(6)/CrSe(5) bilayers are displayed in Fig. 2 (A and B). For the GaAs/CrSe(5)/BST(6) heterostructure, which we refer to as the "bottom" bilayer, no AHE is observed down to a temperature of 2 K. Instead, a linear Hall response of the bottom bilayer indicates the absence of a net magnetization, excluding either an intrinsic AHE in CrSe or an MPE-induced ferromagnetism in BST. In contrast, the GaAs/BST(6)/CrSe(5) bilayer, referred to as the "top" bilayer, shows the results, consistent with a net magnetization induced through an AFM MPE. These results suggest that the top and bottom interfaces of the CrSe/BST/CrSe trilayer structure contribute very differently to the spin transport and magnetic configuration.

In Fig. 2C, the H_c and R_{AHE} are plotted as a function of temperature for the top bilayer, revealing two distinguishable magnetic transition temperatures. The R_{AHE} vanishes above around 120 K, denoting the Curie temperature (T_C) of the MPE-induced ferromagnetism in BST (*7*, *8*). This temperature is comparable to that of most TI/magnetically ordered bilayer systems with ferromagnetic oxides (*7*, *8*). However, another transition temperature is observed at 30 K, which can be attributed to a blocking temperature (T_B), suggesting the possible existence of superparamagnetism (*2*, *26*, *27*). Comparing the temperature dependence of the AHE of the top bilayer with the trilayer shows an excellent agreement between the T_C and T_B (see fig. S4), and is clearly different for the bottom bilayer, which showed no features in the magnetotransport. This suggests that both samples likely exhibit proximity coupling across the top TI/CrSe interface, with identical physical origins for the observed AHE. We also note that the observed T_C is much higher than that of typical Cr-doped BST (*1*, *2*, *4*), so that we may reasonably eliminate the possibility that the ferromagnetism originates from significant Cr interdiffusion. To investigate the presence or absence of MPEs at these two nominally identical interfaces, these systems were probed with

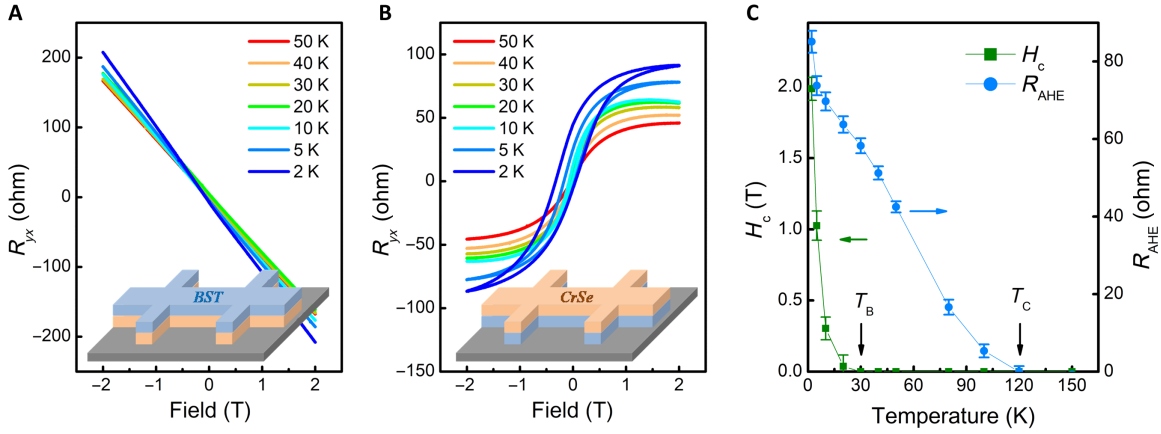

Fig. 2. Magnetotransport for the top and bottom interfaces of CrSe/BST/CrSe. (**A**) R_{yx} curves of the bottom bilayer [CrSe(5)/BST(6)] at various temperatures and (**B**) R_{yx} curves of the top bilayer [BST(6)/CrSe(5)] at various temperatures acquired by applying a 2-T field cooling. The corresponding bilayer structures are shown by insets. (**C**) Plots of H_c and R_{AHE} as functions of temperature for the top bilayer. Curie temperature (T_C) and blocking temperature (T_B) defined by the quenched R_{AHE} and H_c for the top bilayer geometry at 120 and 30 K, respectively, as indicated by the arrows. Error bars represent SD.

soft x-ray absorption spectroscopy (XAS) and polarized neutron reflectometry (PNR) to reconstruct an element-specific, depth-resolved picture of the chemistry and magnetism within the heterostructures. XAS and x-ray magnetic circular dichroism (XMCD) were measured at the Cr $L_{2,3}$-edges (at 584 and 575.3 eV) and are shown in Fig. 3 (A and B) for the top- and bottom-bilayer films, respectively. The XAS and XMCD data were acquired in the total electron yield (TEY) mode at 10 K, with an applied out-of-plane field of 4 T. Incident x-rays were switched from a circular polarization of ±0.9 and traveled along the applied field direction. The XMCD was obtained from the difference in the absorption of consecutive energy scans with two opposite polarizations.

Spectroscopic probing for the origin of interface asymmetry

As shown in Fig. 3 (A and B), although both top and bottom bilayers yielded XMCD on the Cr-edge, indicating ferromagnetic ordering, the dichroism of the top bilayer is significantly larger (~1.55 times) than the bottom. In both cases, we attribute Cr magnetization to a combination of pinned defects in the CrSe bulk and uncompensated spins at the interface (*13*). We postulate that the increased XMCD in the top bilayer indicates the presence of additional spin-polarized moments at the BST/CrSe interface, yielding stronger ferromagnetic exchange interactions and supporting an MPE in BST. To better understand this issue, we examine the fine structure via XAS line shapes shown in Fig. 3C, which compares the Cr $L_{2,3}$-edge XAS for the bottom and top bilayers alongside with the reference spectra of BST, Cr^{2+}, and Cr^{3+} (*28*, *29*). Here, the Cr^{2+} and Cr^{3+} spectra are referred from Figueroa *et al.* (*29*) in Cr-doped BST. Although the top and bottom bilayers show similar general XAS features, a shoulder, highlighted by the dashed line in Fig. 3C, appears in the XAS of the top bilayer, which is not present in the bottom bilayer. A comparison with the reference spectra reveals that the primary Cr valence in both geometries is from Cr^{2+}, while the shoulder feature in the top bilayer can be associated with Cr^{3+}. The mixed-valence Cr^{2+} and Cr^{3+} in the top sample critically changes the magnetic interactions to favor ferromagnetic ordering through a Cr^{2+}-Cr^{3+} double exchange (*30*–*32*). Complementary to this, the absence of any Cr^{3+} contribution in the bottom bilayer suggests a weaker ferromagnetic ordering, representing a critical difference between the two interfaces.

Magnetic profile of the interface via polarized neutrons reflectometry

To determine whether the magnetization observed in the XMCD is localized near the interface, we have performed polarized neutron reflectometry at 5 K in an applied in-plane field of 700 mT on a bare CrSe film and on the top bilayer. Incident and scattered neutrons were polarized either spin-up or spin-down with respect to the applied magnetic field; any net magnetization within the sample will give rise to a difference in the scattering potential, resulting in different reflectivity patterns for the two neutron spin states. A net in-plane magnetization is expected to be set only by the magnetic field, and thus, only the non–spin-flip cross sections (e.g., incident and scattered neutrons have the same spin orientation) were measured. By fitting the reflectivity pattern with a model of the depth-resolved scattering potential, the nuclear and magnetic structure can be determined. Model fitting was performed using the REFL1D software package for χ^2 optimization (*33*). The reflectivity pattern of a CrSe bare film, shown in Fig. 4A, has no apparent splitting between the two neutron spin orientations, as highlighted in the spin asymmetry (Fig. 4B; defined as the difference between the two spin-dependent reflectivities normalized by their summation). The converged depth profile (Fig. 4C) shows the nuclear and magnetic scattering length density (SLD) and confirms that there is no net magnetism in the bulk of the bare film to within the measurement sensitivity of ±2 emu/cm^3 (1 emu/cm^3 = 1 kA m^{-1}; uncertainty, ±1 SD). PNR, however, does not exclude a small magnetization of up to 30 emu/cm^3 in the first few CrSe unit cells near the film surface. We therefore conclude that the majority of the Cr XMCD in Fig. 3A is associated with uncompensated moments at the interface between CrSe and the BST.

Performing PNR on the top bilayer, shown in Fig. 4 (D to F), confirms this interpretation. In this case, a clear splitting is observed with a significant nonzero spin asymmetry. The converged depth profile shows that the reflectometry data can be well described by a magnetization localized at the interface, with a small region of ferromagnetically ordered Cr in the CrSe near the interface and MPE-induced magnetism in the BST. It must be noted that although the interfacial model plotted in Fig. 4F yields an excellent fit to the data, the large interfacial roughness associated with the layered step structure in BST films tends to broaden the magnetization profile in PNR

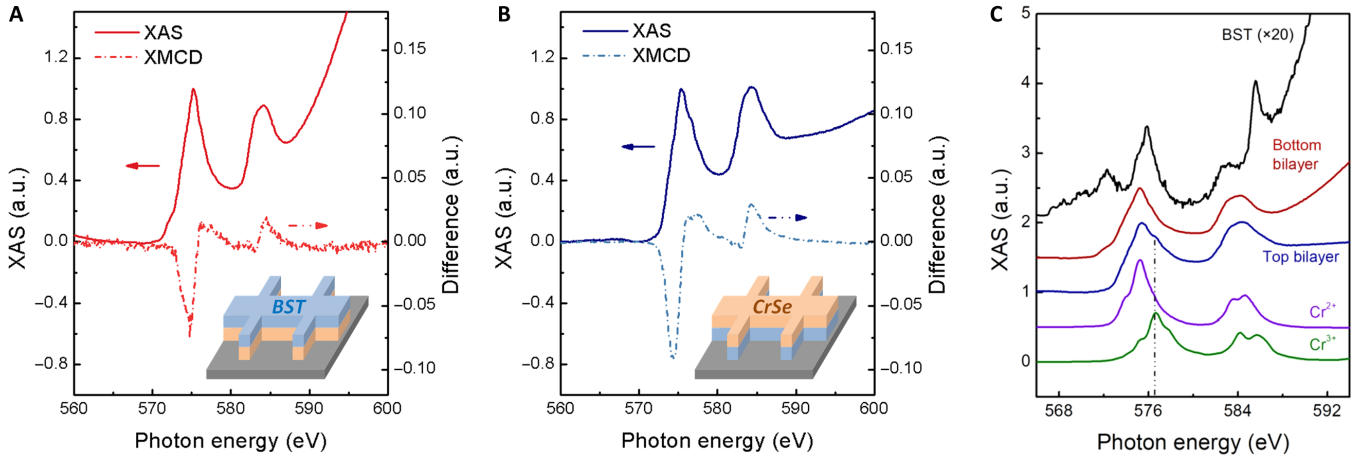

Fig. 3. Electronic and magnetic structures probed by x-ray magnetic spectroscopy. (**A**) XAS and (**B**) XMCD difference at Cr $L_{2,3}$-edge (at 584 and 575.3 eV) in the bottom and top bilayers taken at 10 K, respectively. (**C**) XAS at Cr $L_{2,3}$-edge for the bottom with the top bilayer, alongside with reference spectra of a BST control sample, Cr^{2+} (575.3 eV), and Cr^{3+} (576.5 eV) in Cr-doped Bi_2Se_3 (*29*). Here, we referred the Cr^{2+} and Cr^{3+} reference spectra from the calculation results of Figueroa *et al.*'s work (*29*). The XAS of BST exhibits the Te $M_{4,5}$-edge to define the Te electronic states deviating from the Cr $L_{2,3}$-edge, which is 20 times smaller than the Cr signal. The Cr^{3+} contribution of XAS is as guided by the dash line. a.u., arbitrary units.

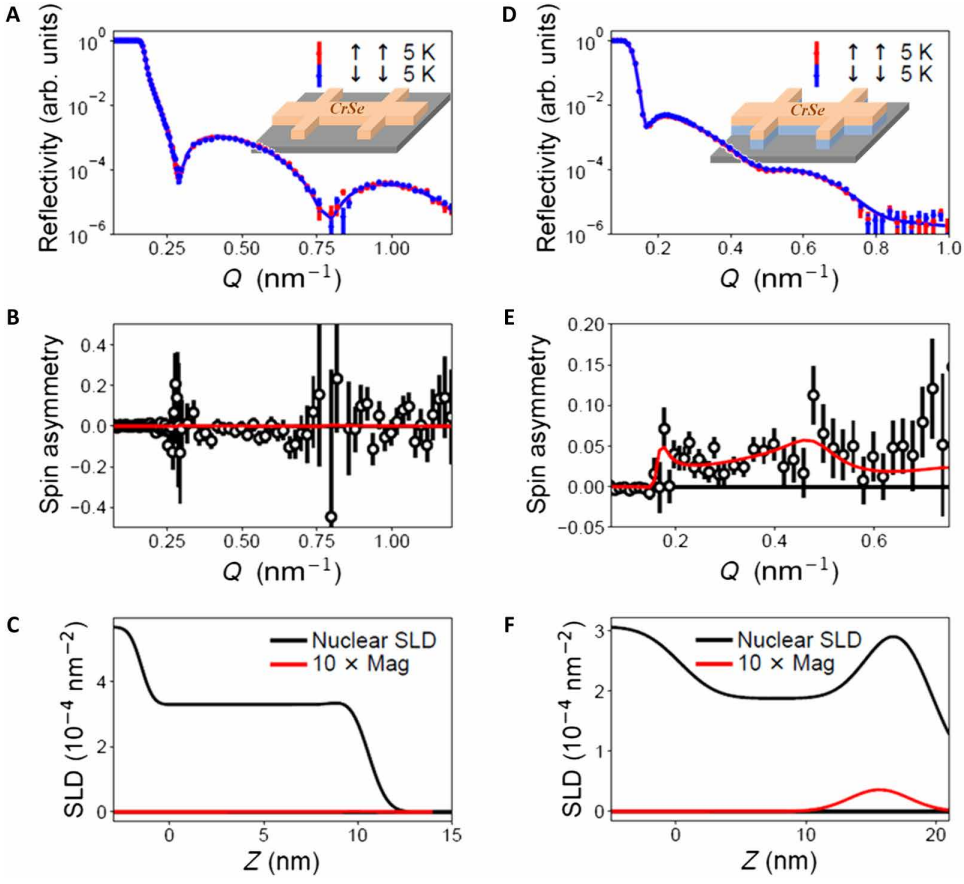

Fig. 4. Magnetic profile at the interface characterized by polarized neutron reflectivity. (**A**) Fitted PNR and (**B**) spin asymmetry for a bare CrSe film. (**C**) Structural and magnetic depth profile used to generate the fit shown for the CrSe film. (**D**) Fitted polarized neutron reflectivity and (**E**) spin asymmetry for a CrSe/$(Bi,Sb)_2Te_3$ heterostructure, along with (**F**) the structural and magnetic depth profile used the generate the fit shown. Measurements were performed in an applied in-plane magnetic field of 700 mT after field cooling to 5 K. Error bars represent SD.

so that it is difficult to determine the precise extent of the magnetic layer. That is, both a magnetic interface (see Fig. 4F) and models with a uniformly magnetized CrSe layer yield extremely similar depth profiles and therefore effectively indistinguishable reflectivity curves. Thus, while PNR demonstrates the emergence of a significant net magnetization consistent with interfacial double exchange and the MPE in the top bilayer, it cannot precisely determine the moment distribution across the heterostructure.

Direct observation on the MPE-induced magnetism in BST

Having demonstrated the clear emergence of a net magnetization in the top bilayer through the x-ray and neutron scattering probes, we can now reexamine the presence and origin of the MPE in the top bilayer. The appearance of Cr^{3+} might be attributable to the population of Cr at or adjacent to the van der Waals gap of BST's surface, specifically the gap at the BST/CrSe interface (*29*). The presence of Cr^{3+} may therefore indicate that the interface of the top bilayer is primarily Cr terminated, so that defects lead to a mixed Cr^{2+}-Cr^{3+} state and enabling a local (2+)-(3+) double-exchange–mediated ferromagnetic order at the interface. On the other hand, the absence of Cr^{3+} in the bottom bilayer reveals a Se-terminated interface, so that the nonmagnetic Se inhibits interfacial exchange interactions and destroys the MPE. Last, we have directly observed MPE-induced ferromagnetism by examining the Sb M_5-edge XAS and XMCD for both bilayers, as shown in Fig. 5 (A and B). Critically, no XMCD is observed in the bottom bilayer, while a significant XMCD on the Sb M_5-edge in the top bilayer suggests the presence of spin-polarized 5p electrons on Sb (*34*–*36*) so that the MPE is confirmed directly, as is the asymmetric MPE effect between the top and bottom interfaces. The spin-polarized Sb orbit enables a local moment in the vicinity of the Fermi level, which electrically dominates the transport property of BST, explaining the sharp difference between the top and bottom interfaces in the original trilayer structure. It must be noted that the XMCD at Sb M_5 and Cr L_3 feature the opposite asymmetries, pointing upward (in Fig. 5B) and downward (in Fig. 3B), respectively. The result suggests that the MPE-induced moment on Sb is ferromagnetically coupled to the neighboring Cr, on the basis of their inverse transition symmetries of Cr L_3 and Sb M_5, i.e., p → d and d → p, respectively (*34*–*36*). This experimental observation is also theoretically supported by our first-principles calculation (see figs. S5 to S7), which also reveal the emergence of a gap in the surface state only for interfaces with Cr termination (S7). Last, Fig. 5C summarizes the results of this study of the two interfaces in the CrSe/BST/CrSe trilayer, as supported by the XAS, XMCD, and PNR results.

DISCUSSION

The realization of either a QAHE based on AFM proximity or of BST-based AFM spintronics, which take advantage of the recently demonstrated terahertz dynamics, requires an AFM with strong interface coupling to BST and the ability to grown high-quality coherent heterostructures (*19*). It is further highly desirable that this AFM be highly insulating in thin-film form so that the BST may be probed unambiguously through transport measurements. In this work, we demonstrate that CrSe meets all of these requirements, having directly detected an MPE induced in BST through interfacial coupling to the AFM CrSe using element-specific magnetic spectroscopy at the Sb M_5-edge. We further show that the MPE is strongly dependent on the symmetry of the interface, with the bottom bilayer CrSe/BST interfaces exhibiting no evidence of MPE, while the top-bilayer

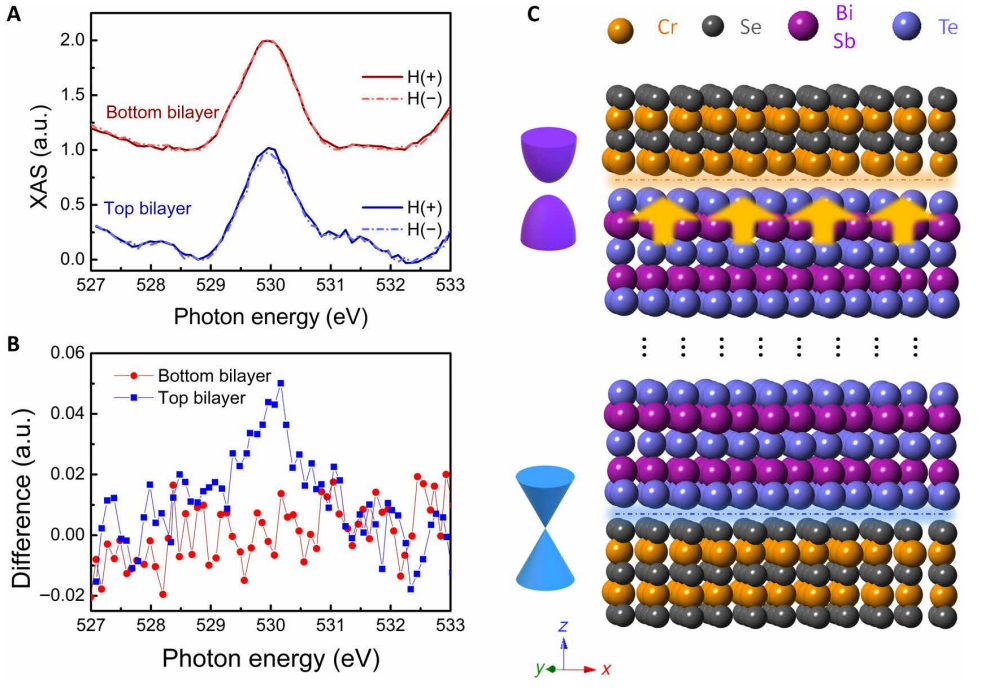

Fig. 5. Direct probe of MPE-induced ferromagnetism in BST studied by magnetic x-ray spectroscopy. (**A**) XAS of Sb M_5-edge (530 eV) probed by applying +4 T and −4 T, denoted as H(+) and H(−), for the bottom and top bilayers. (**B**) XMCD asymmetry of Sb M_5-edge gained from the two XAS in (A). (**C**) Schematic diagram to summarize all results of XAS, XMCD, and PNR. BST is sandwiched by two CrSe layers with Cr(Se)-termination at the top (bottom) interface, respectively. When Cr populates at the top interface, it yields a strong exchange interaction with the adjacent BST and induces a gap at the Dirac cone point to give rise to AHE. Se at the bottom interface magnetically blocks the MPE and topologically preserves the Dirac cone surface state, leading to no detectable magnetism.

BST/CrSe interfaces are magnetized and support an MPE. X-ray magnetic spectroscopy, neutron scattering, and our supplementary theoretical calculations support a picture in which Cr^{3+} is stabilized through the Cr termination of the BST/CrSe interface, leading to (2+)-(3+) double-exchange–mediated interfacial ferromagnetism in CrSe, which couples to the BST and opens a gap in the surface state, as required for the realization of the QAHE. On the other hand, the interfaces of the CrSe/BST bottom bilayer appear to be Se terminated, inhibiting the interlayer exchange coupling. These conclusions are further supported by first-principles calculations, which show these interface terminations to be the lowest energy state and that Cr^{3+} in the van der Waals gap will lead to both a ferromagnetic interface and a magnetized BST with a gap in the topological surface state. Such sensitivity to the interface termination suggests a highly tunable system in which growth rates and techniques may be varied to increase or reduce the disorder at the interface and precisely tune the strength of the exchange coupling. This work identifies key requirements necessary to activate an MPE at the interface of a BST-based exchange-coupled bilayer and provides an ideal model system to explore the fundamental mechanisms behind designing these systems for room temperature functionality.

MATERIALS AND METHODS

Materials

Heterostructures composed of CrSe and $(BiSb)_2Te_3$ in trilayer and bilayer were grown by a molecular beam epitaxial (MBE) technique in an ultrahigh-vacuum PerkinElmer system, with a base pressure at 10^{-8} Pa. GaAs(111) substrate was cleaned by ultrasonic in acetone and then was loaded into the MBE chamber. Before deposition, the substrate was heat-treated at 580°C under a Se-rich atmosphere to remove the native oxide on the surface. After that, the substrate was cooled down to the growth temperatures of 200°C for TI growth and 200°/400°C with two-step growth for CrSe. During the deposition, 6M purity Bi-Sb-Te and Cr-Se elements were coevaporated from Knudsen cells during the TI and CrSe deposition, respectively. The epitaxial growth was in situ monitored by reflection high-energy electron diffraction, which enables growth optimization. All sample preparations were ended up with a 2-nm Al layer in the MBE chamber to prevent samples from air exposure and then were cooled down to the room temperature for following characterizations.

Transport measurement

Samples patterned into a Hall bar structure (1 mm by 0.5 mm) were used for transport measurement by using a physical property measurement system. All the transport measurements were performed after treating a field cooling [±1 T in Fig. 1 (D and E) and +2 T in Fig. 2B], which started above Néel temperature at 300 K and went down to the base temperature (~1.9 K) and recorded the resistance along the longitudinal and transverse directions, R_{xx} and R_{xy}, within one ±2-T magnetic field reversal. For transport measurement, the trilayer was $GaAs_{(111)}$/CrSe (5)/TI (6)/CrSe(5)/Al(2), the CrSe (bottom) bilayer was $GaAs_{(111)}$/CrSe(5)/TI(6)/Al(2), and the CrSe (top) bilayer was $GaAs_{(111)}$/TI(6)/CrSe(5)/Al(2), where the unit of thickness was in nanometers.

X-ray magnetic spectroscopy

XAS and XMCD covering Cr $L_{2,3}$, Sb M_5, and Te $M_{4,5}$-edge were taken using TEY mode for the surface-sensitive and bulk-sensitive probe, respectively. Measurements were performed at beamline 4.0.2 of the Advanced Light Source, Lawrence Berkeley National Laboratory. XMCD spectra were taken at 10 K by varying the incident beam helicity from ±0.9 circular polarizations, denoted as P(+) and P(−), in an applied out-of-plane field of 4 T. The XMCD in this work is presented in difference, which was normalized by XAS L_3-edge intensity. The investigated bottom and top bilayers were capped with Al_2O_3 of 2 nm for protection.

Polarized neutron reflectometry

Samples were field-cooled in an in-plane applied field of 700 mT to a temperature of 5 K. Measurements were performed in the specular reflection geometry, with the direction of wave vector transfer perpendicular to the superlattice surface. The neutron propagation direction was perpendicular to both the sample surface and the applied field direction. On the basis of the strong perpendicular anisotropy of TI films, it is expected that any component of the magnetization not along the field will instead point along the film normal. In this case, neutron scattering selection rules prevent this component of the magnetization from contributing to the scattering and all visible magnetization contributions exclusively parallel to the applied field. Thus, spin-flip scattering is not expected, and we measured only the spin-up and spin-down reflectivities using full polarization analysis to ensure that the incident and scattered beams retained identical neutron polarization directions. We refer, therefore, only to the spin-up and spin-down non–spin-flip reflectivities, which are a function of the nuclear and magnetic SLD profiles. Fitting of the data allows the structural and magnetic depth profiles to be deduced, and modeling was performed using the National Institute of Standards and Technology (NIST) Refl1D software package.

First-principles calculation

The first-principles calculations were performed using VASP (Vienna Ab-initio Simulation Package) based on density functional theory. The convergence was achieved with EDIFF = 10^{-5} control parameter along with k-points matrix of $6 \times 6 \times 1$. The generalized gradient approximation (with Perdew-Burke-Ernzerhof) exchange-correlation function, considering the ion-electron interactions, was used in the calculations. Two structures were modeled in this work: One heterostructure is composed of six Bi_2Te_3 quintuple layer (QLs) on top of CrSe with Bi/Se interface; another heterostructure is composed of CrSe on top of six Bi_2Te_3 QLs with Cr/Te interface. The k-point grids for CrSe(001)/Bi_2Te_3(001) heterostructures with Cr/Te interface and Bi/Se interface was $1 \times 1 \times 1$, which is automatically generated by the Monkhorst-Pack scheme method. The plane-wave cutoff energy was set as 400 eV, and the EDIFF for the electron density self-consistency cycles was 10^{-4} eV. The calculations were supported by superclusters of Henan Normal University.

SUPPLEMENTARY MATERIALS

Supplementary material for this article is available at http://advances.sciencemag.org/cgi/content/full/6/33/eaaz8463/DC1

REFERENCES AND NOTES

1. C.-Z. Chang, J. Zhang, X. Feng, J. Shen, Z. Zhang, M. Guo, K. Li, Y. Ou, P. Wei, L.-L. Wang, Z.-Q. Ji, Y. Feng, S. Ji, X. Chen, J. Jia, X. Dai, Z. Fang, S.-C. Zhang, K. He, Y. Wang, L. Lu, X.-C. Ma, Q.-K. Xue, Experimental observation of the quantum anomalous Hall effect in a magnetic topological insulator. *Science* **340**, 167–170 (2013).

2. W. Wang, Y. Ou, C. Liu, Y. Wang, K. He, Q.-K. Xue, W. Wu, Direct evidence of ferromagnetism in a quantum anomalous Hall system. *Nat. Phys.* **14**, 791–795 (2018).
3. X. Kou, L. Pan, J. Wang, Y. Fan, E. S. Choi, W.-L. Lee, T. Nie, K. Murata, Q. Shao, S.-C. Zhang, K. L. Wang, Metal-to-insulator switching in quantum anomalous Hall states. *Nat. Commun.* **6**, 8474 (2015).
4. C.-Z. Chang, M. Li, Quantum anomalous Hall effect in time-reversal-symmetry breaking topological insulators. *J. Phys. Condens. Matter* **28**, 123002 (2016).
5. C. Tang, C.-Z. Chang, G. Zhao, Y. Liu, Z. Jiang, C.-X. Liu, M. R. McCartney, D. J. Smith, T. Chen, J. S. Moodera, J. Shi, Above 400-K robust perpendicular ferromagnetic phase in a topological insulator. *Sci. Adv.* **3**, e1700307 (2017).
6. M. Lang, M. Montazeri, M. C. Onbasli, X. Kou, Y. Fan, P. Upadhyaya, K. Yao, F. Liu, Y. Jiang, W. Jiang, K. L. Wong, G. Yu, J. Tang, T. Nie, L. He, R. N. Schwartz, Y. Wang, C. A. Ross, K. L. Wang, Proximity induced high-temperature magnetic order in topological insulator - ferrimagnetic insulator heterostructure. *Nano Lett.* **14**, 3459–3465 (2014).
7. Z. Jiang, C.-Z. Chang, C. Tang, P. Wei, J. S. Moodera, J. Shi, Independent tuning of electronic properties and induced ferromagnetism in topological insulators with heterostructure approach. *Nano Lett.* **15**, 5835–5840 (2015).
8. X. Che, K. Murata, L. Pan, Q. L. He, G. Yu, Q. Shao, G. Yin, P. Deng, Y. Fan, B. Ma, X. Liang, B. Zhang, X. Han, L. Bi, Q.-H. Yang, H. Zhang, K. L. Wang, Proximity-induced magnetic order in a transferred topological insulator thin film on a magnetic insulator. *ACS Nano* **12**, 5042–5050 (2018).
9. C.-Y. Yang, Y.-H. Lee, K.-H. O. Yang, K.-C. Chiu, C. Tang, Y. Liu, Y.-F. Zhao, C.-Z. Chang, F.-H. Chang, H.-J. Lin, J. Shi, M.-T. Lin, Direct observation of proximity-induced magnetism and spin reorientation in topological insulator on a ferrimagnetic oxide. *Appl. Phys. Lett.* **114**, 082403 (2018).
10. F. Katmis, V. Lauter, F. S. Nogueira, B. A. Assaf, M. E. Jamer, P. Wei, B. Satpati, J. W. Freeland, I. Eremin, D. Heiman, P. Jarillo-Herrero, J. S. Moodera, A high-temperature ferromagnetic topological insulating phase by proximity coupling. *Nature* **533**, 513–516 (2016).
11. R. Watanabe, R. Yoshimi, M. Kawamura, M. Mogi, A. Tsukazaki, X. Z. Yu, K. Nakajima, K. S. Takahashi, M. Kawasaki, Y. Tokura, Quantum anomalous Hall effect driven by magnetic proximity coupling in all-telluride based heterostructure. *Appl. Phys. Lett.* **115**, 102403 (2019).
12. M. Charilaou, F. Hellman, Roughness effects in uncompensated antiferromagnets. *J. Appl. Phys.* **117**, 083907 (2015).
13. H. Ohldag, A. Scholl, F. Nolting, E. Arenholz, S. Maat, A. T. Young, M. Carey, J. Stöhr, Correlation between exchange bias and pinned interfacial spins. *Phys. Rev. Lett.* **91**, 017203 (2003).
14. Q. L. He, X. Kou, A. J. Grutter, G. Yin, L. Pan, X. Che, Y. Liu, T. Nie, B. Zhang, S. M. Disseler, B. J. Kirby, W. R. Ii, Q. Shao, K. Murata, X. Zhu, G. Yu, Y. Fan, M. Montazeri, X. Han, J. A. Borchers, K. L. Wang, Tailoring exchange couplings in magnetic topological-insulator/antiferromagnet heterostructures. *Nat. Mater.* **16**, 94–101 (2017).
15. Q. L. He, G. Yin, A. J. Grutter, L. Pan, X. Che, G. Yu, D. A. Gilbert, S. M. Disseler, Y. Liu, P. Shafer, B. Zhang, Y. Wu, B. J. Kirby, E. Arenholz, R. K. Lake, X. Han, K. L. Wang, Exchange-biasing topological charges by antiferromagnetism. *Nat. Commun.* **9**, 2767 (2018).
16. Q. L. He, G. Yin, L. Yu, A. J. Grutter, L. Pan, C.-Z. Chen, X. Che, G. Yu, B. Zhang, Q. Shao, A. L. Stern, B. Casas, J. Xia, X. Han, B. J. Kirby, R. K. Lake, K. T. Law, K. L. Wang, Topological transitions induced by antiferromagnetism in a thin-film topological insulator. *Phys. Rev. Lett.* **121**, 096802 (2018).
17. O. Gomonay, V. Baltz, A. Brataas, Y. Tserkovnyak, Antiferromagnetic spin textures and dynamics. *Nat. Phys.* **14**, 213–216 (2018).
18. C. Song, Y. You, X. Chen, X. Zhou, Y. Wang, F. Pan, How to manipulate magnetic states of antiferromagnets. *Nanotechnology* **29**, 112001 (2018).
19. J. Li, C. B. Wilson, R. Cheng, M. Lohmann, M. Kavand, W. Yuan, M. Aldosary, N. Agladze, P. Wei, M. S. Sherwin, J. Shi, Spin current from sub-terahertz-generated antiferromagnetic magnons. *Nature* **578**, 70–74 (2020).
20. L. Šmejkal, Y. Mokrousov, B. Yan, A. H. MacDonald, Topological antiferromagnetic spintronics. *Nat. Phys.* **14**, 242–251 (2018).
21. Q. Shao, A. Grutter, Y. Liu, G. Yu, C.-Y. Yang, D. A. Gilbert, E. Arenholz, P. Shafer, X. Che, C. Tang, M. Aldosary, A. Navabi, Q. L. He, B. J. Kirby, J. Shi, K. L. Wang, Exploring interfacial exchange coupling and sublattice effect in heavy metal/ferrimagnetic insulator heterostructures using Hall measurements, x-ray magnetic circular dichroism, and neutron reflectometry. *Phys. Rev. B* **99**, 104401 (2018).
22. S. Polesya, S. Mankovsky, D. Benea, H. Ebert, W. Bensch, Finite-temperature magnetism of CrTe and CrSe. *J. Phys. Condens. Matter* **22**, 156002 (2010).
23. L. M. Corliss, N. Elliott, J. M. Hastings, R. L. Sass, Magnetic structure of chromium selenide. *Phys. Rev.* **122**, 1402–1406 (1961).
24. S. Zhong, D. Jun, Z. Shi-Ming, Exchange bias in ferromagnet/antiferromagnet bilayers. *China Phys. B* **23**, 027503 (2014).
25. I. V. Roshchin, O. Petracic, R. Morales, Z.-P. Li, X. Batlle, I. K. Schuller, Lateral length scales in exchange bias. *Purophys. Lett.* **71**, 297–303 (2005).
26. C.-Y. Yang, S.-J. Chang, M.-H. Lee, K.-H. Shen, S.-Y. Yang, H.-J. Lin, Y.-C. Tseng, Competing anisotropy-tunneling correlation of the CoFeB/MgO perpendicular magnetic tunnel junction: An electronic approach. *Sci. Rep.* **5**, 17169 (2015).
27. E. O. Lachman, A. F. Young, A. Richardella, J. Cuppens, H. R. Naren, Y. Anahory, A. Y. Meltzer, A. Kandala, S. Kempinger, Y. Myasoedov, M. E. Huber, N. Samarth, E. Zeldov, Visualization of superparamagnetic dynamics in magnetic topological insulators. *Sci. Adv.* **1**, e1500740 (2015).
28. R. Cheng, C. N. Borca, P. A. Dowben, S. Stadler, Y. U. Idzerda, Potential phase control of chromium oxide thin films prepared by laser-initiated organometallic chemical vapor deposition. *Appl. Phys. Lett.* **78**, 521–523 (2001).
29. A. I. Figueroa, G. van der Laan, L. J. Collins-McIntyre, S.-L. Zhang, A. A. Baker, S. E. Harrison, P. Schönherr, G. Cibin, T. Hesjedal, Magnetic Cr doping of Bi_2Se_3: Evidence for divalent Cr from x-ray spectroscopy. *Phys. Rev. B* **90**, 134402 (2014).
30. S. Zhang, L. Pi, W. Tong, S. Tan, C. Zhang, Y. Zhang, Cr enhanced ferromagnetism in $La_{0.5}Ba_{0.5}CoO_3$ due to possible double-exchange interaction. *J. Alloys Compd.* **628**, 251–256 (2015).
31. P. Schlottmann, Double-exchange mechanism for CrO_2. *Phys. Rev. B* **67**, 174419 (2003).
32. M. J. R. Hoch, P. L. Kuhns, W. G. Moulton, A. P. Reyes, M. A. Torija, J. F. Mitchell, C. Leighton, Disorder and double-exchange spin dynamics in $La_{0.7}Sr_{0.3}MnO_3$ and $La_{0.7}Sr_{0.3}CoO_3$ from NMR hyperfine couplings. *Phys. Rev. B* **75**, 104421 (2007).
33. B. J. Kirby, P. A. Kienzle, B. B. Maranville, N. F. Berk, J. Krycka, F. Heinrich, C. F. Majkrzak, Phase-sensitive specular neutron reflectometry for imaging the nanometer scale composition depth profile of thin-film materials. *Curr. Opin. Colloid Interface Sci.* **17**, 44–53 (2012).
34. M. Ye, W. Li, S. Zhu, Y. Takeda, Y. Saitoh, J. Wang, H. Pan, M. Nurmamat, K. Sumida, F. Ji, Z. Liu, H. Yang, Z. Liu, D. Shen, A. Kimura, S. Qiao, X. Xie, Carrier-mediated ferromagnetism in the magnetic topological insulator Cr-doped $(Sb,Bi)_2Te_3$. *Nat. Commun.* **6**, 8913 (2015).
35. L. B. Duffy, A. I. Figueroa, Ł. Gładczuk, N.-J. Steinke, K. Kummer, G. van der Laan, T. Hesjedal, Magnetic proximity coupling to Cr-doped Sb_2Te_3 thin films. *Phys. Rev. B* **95**, 224422 (2017).
36. A. Kimura, S. Suga, T. Shishidou, S. Imada, T. Muro, S. Y. Park, T. Miyahara, T. Kaneko, T. Kanomata, Magnetic circular dichroism in the soft-x-ray absorption spectra of Mn-based magnetic intermetallic compounds. *Phys. Rev. B* **56**, 6021–6030 (1997).

Acknowledgments

Funding: This work is supported as part of the Spins and Heat in Nanoscale Electronic Systems (SHINES), an Energy Frontier Research Center funded by the U.S. Department of Energy (DOE), Office of Science, Basic Energy Sciences (BES), under award no. DE-SC0012670. We acknowledge the support from the Army Research Office Multidisciplinary University Research Initiative (MURI) program accomplished under grant nos. W911NF-16-1-0472 and W911NF-15-1-10561. C.-Y.Y. would like to thank the support by the Ministry of Science and Technology (MoST), Taiwan, under grant no. 106-2917-I-564-062. Q.L.H. acknowledges the supports from the National Natural Science Foundation of China (grant no. 11874070), the National Key R&D Program of China (grant no. 2018YFA0305601), the Strategic Priority Research Program of Chinese Academy of Sciences (grant no. XDB28000000), and the National Thousand-Young Talents Program in China. This research used resources of the Advanced Light Source, a U.S. DOE Office of Science User Facility under contract no. DE-AC02-05CH11231. **Author contributions:** L.P., C.-Y.Y., and K.L.W. coconceived and designed this study. L.P. took charge of materials and transport characterizations with the assistance of X.C. E.A., A.J.G., D.A.G., and P.S. collected the XAS-XMCD data at the Advanced Light Source, Lawrence Berkeley National Laboratory. C.-Y.Y. and A.J.G. were responsible for the XAS-XMCD analyses. H.W. dealt with the first-principles calculation for the moment profile and the formation energy of the system. Q.L.H., Y.W., P.D., and G.Y. were responsible for the fundamental characterizations and the elaboration on transport property for CrSe. A.J.G. performed and analyzed the polarized neutron reflectometry. A.J.G., D.A.G., J.A.B., and W.R. performed the neutron diffraction. C.-Y.Y., L.P., and A.J.G. organized the data presentation and drafted the manuscript under the supervision of K.L.W. All the authors reviewed and commented on this manuscript. **Competing interests:** The authors declare that they have no competing interests. Certain commercial equipment, instruments, or materials are identified in this paper to foster understanding. Such identification does not imply recommendation or endorsement by the National Institute of Standards and Technology, nor does it imply that the materials or equipment identified is necessarily the best available for the purpose. **Data and materials availability:** All data needed to evaluate the conclusions in the paper are present in the paper and/or the Supplementary Materials. Additional data related to this paper may be requested from the authors.

Submitted 14 October 2019
Accepted 26 June 2020
Published 12 August 2020
10.1126/sciadv.aaz8463

Citation: C.-Y. Yang, L. Pan, A. J. Grutter, H. Wang, X. Che, Q. L. He, Y. Wu, D. A. Gilbert, P. Shafer, E. Arenholz, H. Wu, G. Yin, P. Deng, J. A. Borchers, W. Ratcliff II, K. L. Wang, Termination switching of antiferromagnetic proximity effect in topological insulator. *Sci. Adv.* **6**, eaaz8463 (2020).